



# Effect of Cooling Rate on Precipitation Behavior of Al–7.65Zn–2.59Mg–1.95Cu Alloy with Minor Elements of Zr and Ti

Saif Haider Kayani<sup>1,2</sup> · Jae-Gil Jung<sup>1</sup> · Min-Seok Kim<sup>1</sup> · Kwangjun Euh<sup>1,2</sup>

Received: 4 April 2019 / Accepted: 15 July 2019 / Published online: 27 July 2019  
© The Korean Institute of Metals and Materials 2019

## Abstract

We investigate the effect of cooling rate on the precipitation behavior during cooling from solution treatment temperature and post-aging of a high-strength Al–7.65Zn–2.59Mg–1.95Cu–0.11Zr–0.04Ti extruded alloy. Solution treatment at 450 °C caused the partial dissolution and disintegration of  $\eta$  phase, along with a partial recrystallization of Al grains. The formation of fine  $L1_2$ -type  $Al_3Zr/Al_3(Zr,Ti)$  (~ 20 nm) and relatively large Ti-rich dispersoids (~ 100 nm) took place during extrusion and/or solution treatment processes. The slow cooling from solution treatment temperature (0.3 °C/min) caused the precipitation of  $\eta$  phases on coarse  $Al_3(Zr,Ti)$  particles (formed during solidification), Ti-rich dispersoids (formed during extrusion/solution treatment), grain boundaries, and grain interiors, thereby resulting in negligible aging responses during post-aging at room and elevated temperatures. During fast cooling at 850 °C/min, however, the  $\eta$  phases did not precipitate and thus the Al matrix remained supersaturated, leading to significant aging responses by the formation of GP zones and metastable  $\eta''/\eta'$  precipitates.

**Keywords** Aluminum alloy · Precipitation · Microstructure · Transmission electron microscopy (TEM)

## 1 Introduction

Due to their superior mechanical properties, 7xxx series Al alloys have been widely used in structural applications for the aerospace and automotive industries [1–5]. These alloys are precipitation hardenable Al–Zn–Mg–Cu alloys and their precipitation behaviors, occurring during the aging process after solution treatment, have been extensively studied [6–8]. The cooling rate from solution treatment temperature is used to define the quench sensitivity, which is defined as loss or change in properties due to reduced quenching rate [9]. In terms of microstructure, quench sensitivity is associated with nucleation sites of precipitates such as grain boundaries, sub-grain boundaries, dispersoids, and dislocations [10]. The quench sensitivity can be controlled by decreasing the contents of alloying elements (e.g., Zn, Mg, Cu);

however, this is likely to cause deterioration of the properties [6, 7].

Many studies [6–16] have reported on precipitation behavior during cooling of Al–Zn–Mg–Cu alloys containing a minor element of Zr. Godard et al. [10] reported the heterogeneous precipitation of  $\eta$  precipitates on cuboidal  $Al_3Zr$  dispersoids during quenching of a cold-rolled Al–6.0Zn–2.3Mg–1.7Cu alloy. Deschamps et al. [11] observed quench-induced precipitates in an Al–4.6Zn–1.2Mg–0.1Cu alloy and reported the formation of coarse  $\eta$  precipitates (200 nm) along grain boundaries and on dispersoids in the grain interior at relatively high temperatures (320–220 °C) and fine plate-like  $\eta$  precipitates (7–10 nm) in the grain interior at low temperatures below 200 °C. Liu et al. [12] also reported the formation of lath-shaped  $\eta$  particles on pre-existing incoherent  $Al_3Zr$  dispersoids during quenching of a hot-rolled Al–7.9Zn–2.2Mg–2.1Cu–0.15Zr alloy. According to previous articles, quench-induced precipitation can be classified as coarse precipitates that form heterogeneously at grain boundaries, subgrain boundaries, dislocations, and dispersoids at high temperatures of 350–250 °C and fine precipitates that form homogeneously in the grain interior at relatively low temperatures of 250–100 °C.

✉ Kwangjun Euh  
keuh@kims.re.kr

<sup>1</sup> Metallic Materials Division, Korea Institute of Materials Science, Changwon 51508, Republic of Korea

<sup>2</sup> Advanced Materials Engineering, Korea University of Science and Technology (UST), Daejeon 34113, Republic of Korea

Both heterogeneous and homogenous precipitates that form during cooling can affect the age-hardening behavior of 7xxx Al alloys [17]. This is based on the reduced amount of solutes (e.g., Zn, Mg, Cu) available for precipitation during subsequent aging, as well as the coarsening of quench-induced precipitates [18]. For instance, Liu et al. [12] reported that, with a decrease of the cooling rate from 170 to 2 °C/s, the hardness of hot-rolled Al–7.9Zn–2.2Mg–2.1Cu–0.2Zr alloy decreases from 202 to 159 HV after aging at 121 °C for 24 h.

Recently, alloying elements such as Ti [19], Sc [20], Y [21], and Hf [22] have also been used in 7xxx alloys to further improve the mechanical properties. Gao et al. [19] reported that the addition of 0.2 wt%Ti to an Al–6Zn–2Mg–2.5Cu–0.2Zr alloy reduced the coarsening rate of L<sub>1</sub><sub>2</sub> dispersoids and accelerated the precipitation kinetics during aging. According to the literature on Al–Ti binary [23] and Al–Ti–Zr [24, 25] ternary systems, it is expected that the addition of Ti can cause the formation of a new Ti-containing phase (e.g., Al<sub>3</sub>Ti). However, there have been few reports on the formation of new dispersoids in 7xxx Al alloys containing Zr and Ti elements and their roles in the precipitation behavior during cooling and artificial aging. Therefore, the present study aimed to investigate the formation of dispersoids and their role in the precipitation behavior during cooling of an Al–Zn–Mg–Cu alloy containing a small amount of Zr and Ti. In addition, the effects of cooling rate on the aging behavior at room and elevated temperatures were examined.

## 2 Experimental Procedure

A 10-kilogram alloy melt was prepared in an electric resistance furnace at 720 °C using high purity (99.9%) metals (Al, Zn, and Mg) and master alloys (Al–30Cu and Al–5Zr); melt was then degassed via Ar gas bubbling filtration for 10 min. After 1.5 kg of the melt was ultrasonically treated with a Ti sonotrode for 1 min over a temperature range of 760–720 °C, the melt was poured at 720 °C into a cylindrical mold (Ø55 × 200 mm) preheated to 180 °C. Using inductively coupled plasma optical emission spectrometry (ICP-OES, Thermo Electron, ICAP6500), the chemical composition of the as-cast ingot was determined to be Al–7.65 Zn–2.59Mg–1.95Cu–0.11Fe–0.03Si–0.11Zr–0.04Ti (wt %).

A billet (Ø50 × 200 mm) for direct extrusion was machined from the as-cast ingot. The billet was preheated to 500 °C for 10 min and then extruded at an extrusion ratio of 25: 1 at a ram speed of 0.8 mm/s and pressure of 120–140 MPa. The container and die of the extrusion press were preheated to 430 °C and 500 °C before extrusion. The extruded rod, with a diameter of 10 mm, was cooled in air at room temperature.

Three types of specimens with dimensions of Ø10 mm × t mm (t = 10, 0.6) were prepared from the extruded rod for heat treatment. The specimens were solution-treated at 450 °C for 24 h in a box furnace and then quenched in water or slowly cooled in the furnace. The cooling rate from 450 °C to room temperature was measured as 850 °C/min for water-quenching (WQ) and 0.3 °C/min for furnace cooling (FC). The solution-treated specimens were then naturally aged (NA) at 25 °C ± 2 up to 1000 h or artificially aged (AA) at 120 °C for the holding times of 1 and 4 h.

After the specimens were mechanically polished, their microstructures were observed using scanning electron microscopy (SEM, JEOL, JSM6610LV) and energy dispersive X-ray spectroscopy (EDS). Grain structure was observed using an electron backscattered diffraction (EBSD) apparatus installed in the SEM (TESCAN, MIRA 1 LMH) with a step size of 6 µm. The precipitates were examined using a transmission electron microscope (TEM, JEOL, JEM2100F) and EDS operated at 200 kV. TEM specimens were prepared using a Zet-polisher (Struers, TenuPol 5) at a voltage of 20 V in a mixed solution of methyl alcohol and nitric acid (3:1) cooled to –25 °C.

Differential scanning calorimetry (DSC, Perkin-Elmer, Pyris diamond) was used to examine the precipitation behavior. DSC specimens with weights of approximately 30 mg were heated to 550 °C at a rate of 10 °C/min in Ar atmosphere. The hardness of the Al matrix was measured using a Vickers hardness tester (Mitutoyo, Model HM-122) under a load of 0.3 kg and dwell time of 15 s. The electrical resistivity of the specimens (Ø10 × 0.6 mm) was measured at room temperature using a voltmeter (Keithley, Model2182) and a sourcemeter (Keithley, Model6220) according to ASTM standard F76 08 [26].

## 3 Results and Discussions

### 3.1 Microstructure

Figure 1a shows the SEM image of center of the as-cast alloy, the microstructure exhibits dendritic morphology with continuous network of Al/η eutectic phase inside α-Al matrix. Figure 1b shows an SEM image of secondary phases aligned along the extrusion direction (ED) of the extruded alloy. It was confirmed by compositional analysis given in Table 1 that continuous bands of second phases are η-phase, while coarse irregular particles are Al<sub>7</sub>Cu<sub>2</sub>Fe particles. The extruded alloy also contained fine η particles and a small amount of Mg<sub>2</sub>Si particles. Figure 1c shows an SEM image of the WQ alloy after solution treatment at 450 °C for 24 h. Most of the fine η particles observed in the extruded alloy were dissolved during solution treatment, although there are some

**Fig. 1** SEM images of **a** as-cast ingot, **b** as-extruded alloy, and **c** WQ and **d** FC alloys after solution treatment

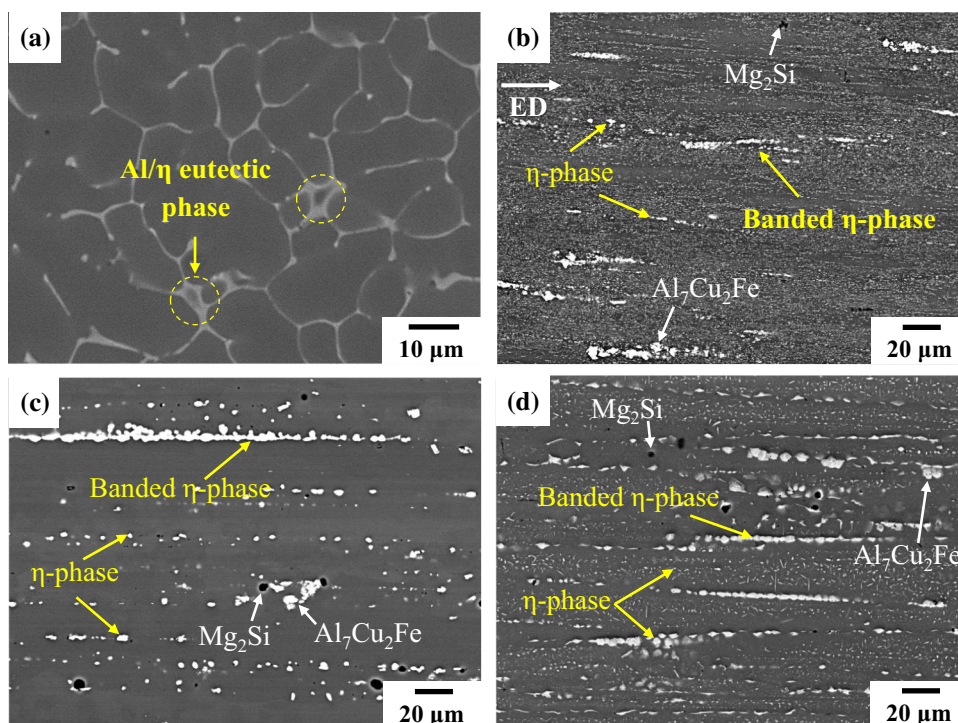


**Table 1** EDS results of precipitates formed in WQ and FC alloys

Alloy	Phase	Chemical composition (wt%)					
		Mg	Zn	Cu	Zr	Ti	Al
WQ	Coarse $\text{Al}_3(\text{Zr,Ti})$	1.94	2.41	2.16	9.02	3.11	Bal.
	Fine $\text{Al}_3(\text{Zr,Ti})$	1.41	5.12	3.19	16.3	7.68	Bal.
	Ti-rich particle	17.43	0.23	0.11	–	11.32	Bal.
	Al matrix	0.86	3.97	0.73	0.24	0.21	Bal.
FC	Coarse $\text{Al}_3(\text{Zr,Ti})$	12.74	33.86	6.57	8.24	7.33	Bal.
	Fine $\text{Al}_3(\text{Zr,Ti})$	3.21	7.8	2.77	15.4	8.64	Bal.
	Ti-rich particle	18.37	0.40	0.08	–	12.5	Bal.
	$\eta$ -Phase (on Ti-rich)	15.37	10.97	2.19	–	–	Bal.
	$\eta$ -Phase (in Al matrix)	13.35	33.82	3.33	–	–	Bal.
	Al matrix	0.22	0.64	0.13	0.20	0.18	Bal.

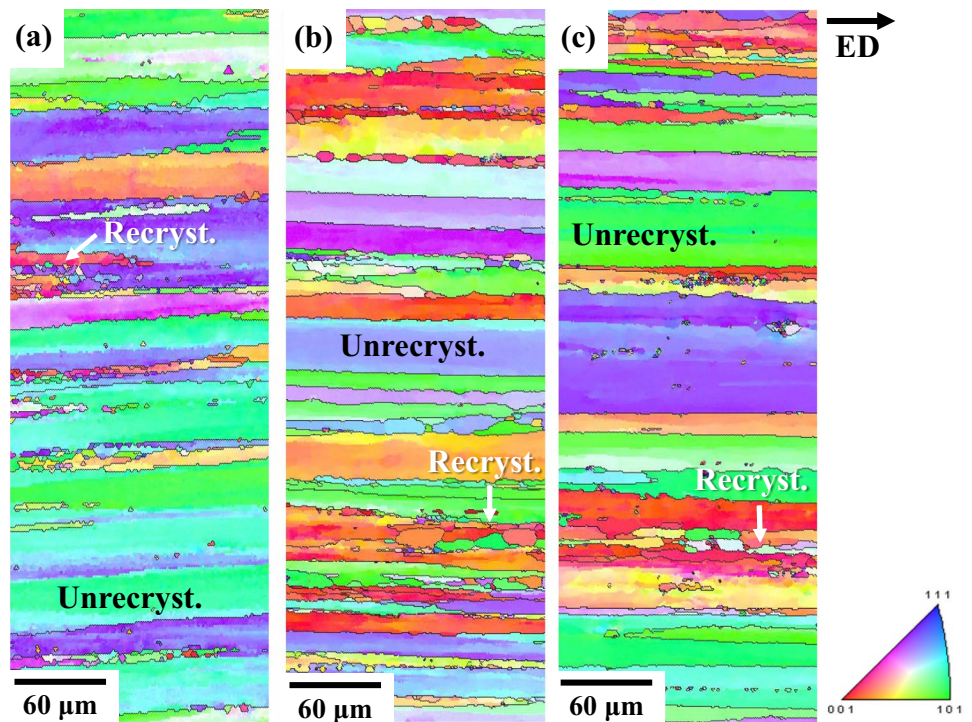
undissolved  $\eta$ -phase and  $\text{Al}_7\text{Cu}_2\text{Fe}$  particles. Meanwhile, the FC alloy contains numerous fine  $\eta$  particles in addition to undissolved  $\eta$ -phase and  $\text{Al}_7\text{Cu}_2\text{Fe}$  particles, as shown in Fig. 1d. Figure 2a–c show the inverse pole figure (IPF) of as-extruded WQ and FC alloys. The grain structure of three alloys exhibits elongated grains along the ED. Fine grains with sizes less than 30  $\mu\text{m}$  are grains that were recrystallized during extrusion and/or solution treatment. Due to the additional static recrystallization occurring during the solution treatment process, the size and area fraction of recrystallized grains were larger in the WQ and FC alloys compared to the extruded alloy. There is no difference in the grain structure between the WQ and FC

alloys, indicating that recrystallization during cooling is negligible.

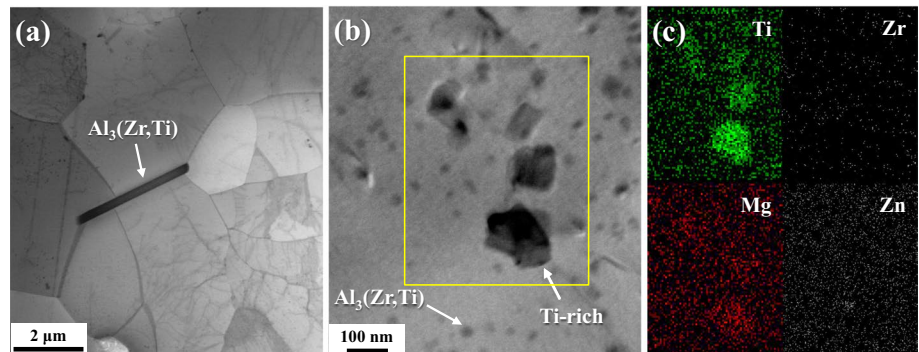
### 3.2 Formation of Dispersoids

Figure 3a shows a TEM image of the WQ alloy after natural aging for 100 h. There is a large particle with size of approximately 4  $\mu\text{m}$  at the grain boundary; this particle contains Zr and Ti elements (see Table 1). It is thought that the large particle is an  $\text{Al}_3(\text{Zr,Ti})$  phase that formed during solidification and moved to the grain boundary during extrusion.  $\text{Al}_3(\text{Zr,Ti})$  particles with diameters of a few hundreds of nanometers were also present at grain boundaries and

**Fig. 2** Inverse pole figure map of **a** as-extruded alloy and **b** WQ and **c** FC alloys after solution treatment



**Fig. 3** TEM images of WQ alloy showing the presence of **a** coarse  $\text{Al}_3(\text{Zr,Ti})$  along grain boundaries and **b** fine  $\text{Al}_3(\text{Zr,Ti})$  and Ti-rich particles at grain interior. **c** EDS element mapping of **b**



are considered to have formed during hot extrusion and/or solution treatment at 450 °C.

There are cuboidal particles and fine spherical particles in the grain interior, as shown in (Fig. 3b). Elemental mapping (Fig. 3c) and point (Table 1) analyses indicate that the cuboidal particles contain Ti and Mg elements and do not contain Zr element. The chemical composition of the cuboidal particle is different from that of the dispersoids previously reported in Al–Ti [23] binary and Al–Ti–Zr [24, 25] ternary systems.

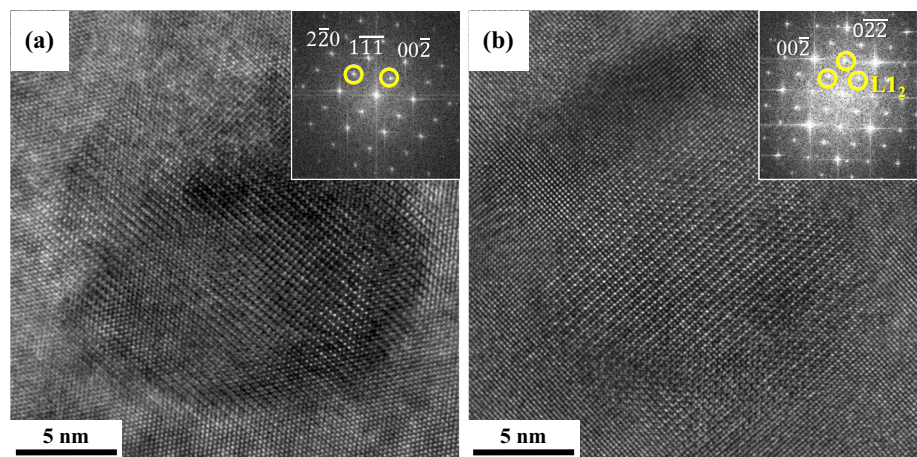
Figure 4a, b show typical high-resolution TEM (HRTEM) images of fine spherical particles in the Al matrix taken at  $[110]\text{Al}$  and  $[100]\text{Al}$  directions. The corresponding fast Fourier transformation (FFT) results show super lattice spots at the  $(00\bar{1})\text{Al}$  and  $(01\bar{1})\text{Al}$  planes, indicating that the fine spherical particles have a  $\text{L1}_2$  structure and are coherent

with the Al matrix. EDS results (Table 1) indicate that the  $\text{L1}_2$ -type particles are  $\text{Al}_3(\text{Zr}_{0.7},\text{Ti}_{0.3})$ . According to previous articles [11, 27], due to the low diffusion coefficient of Zr in the Al matrix, the formation of  $\text{L1}_2$ -type  $\text{Al}_3\text{Zr}$  occurs at temperatures higher than 450 °C. Thus, it is considered that most  $\text{L1}_2$ - $\text{Al}_3(\text{Zr,Ti})$  particles are formed during hot extrusion and solution treatment at 450 °C for a long time of 24 h.

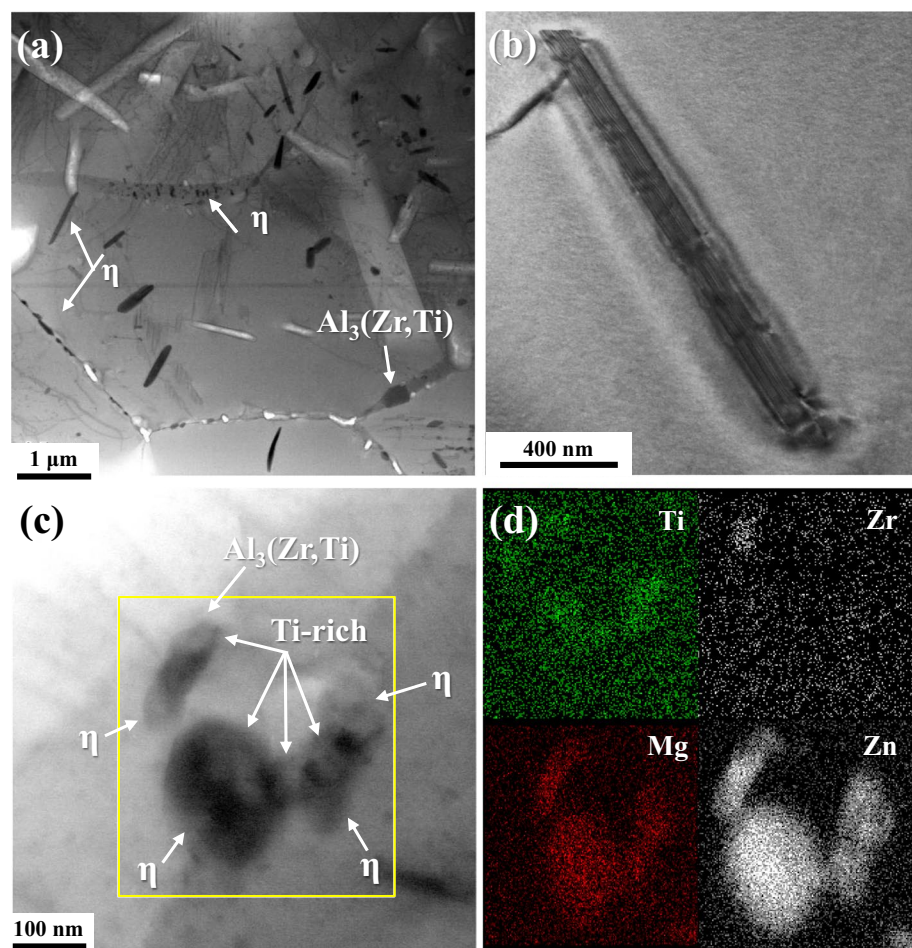
### 3.3 Precipitation During Cooling

Figure 5a shows a TEM image of the FC alloy which contains coarse  $\text{Al}_3(\text{Zr,Ti})$  particles at the grain boundaries like the WQ alloy. However, the contents of Zn, Mg, and Cu in the  $\text{Al}_3(\text{Zr,Ti})$  particles of the FC alloy are much higher than those of the WQ alloy (Table 1). This means that  $\eta$  phases were formed on the  $\text{Al}_3(\text{Zr,Ti})$  particles during slow cooling.

**Fig. 4** Typical HRTEM image and FFT results of  $L1_2$  phases taken at **a**  $[110]Al$  and **b**  $[100]Al$



**Fig. 5** TEM images showing the presence of  $\eta$  phase **a** at grain boundaries/interior, **b** in Al matrix, and **c** on dispersoids in the FC alloy. **d** EDS element mapping of **b**



In addition,  $\eta$  precipitates with size of 200–500 nm are present along the grain boundaries and in the grain interior. Figure 5b provides a TEM image of the rod-shaped  $\eta$  phase formed in the Al matrix. TEM observation indicates that the longitudinal axis of the rod-shaped  $\eta$  precipitate is parallel to  $[010]Al$ . It can be seen that the length of the precipitate is quite larger than the width, suggesting that homogenous

growth of these precipitates along this direction took place during the cooling process. The cuboidal particles containing Ti and Mg also act as preferential nucleation sites of the  $\eta$  phase, which is evidenced in Fig. 5c, d.

On the other hand,  $\eta$  precipitates were not observed in the WQ alloy, indicating that the Al matrix of the WQ alloy contains more solute atoms than does the FC alloy. This can

be supported by the higher concentrations of Zn, Mg, and Cu in the Al matrix of the WQ alloy (see Table 1).

### 3.4 Effect of Cooling Rate on Aging Behavior

Figure 6a, b show variations in hardness and electrical resistivity with natural aging time for the WQ and FC alloys. The hardness and electrical resistivity values of the WQ alloy were 70 HV and 51 nΩm, respectively; both increased sharply to 150 HV and 58 nΩm during natural aging. Electrical resistivity is highly dependent upon cluster/GP zones, they are very effective in scattering electron during resistivity test leading to high resistivity values. The times to reach peak hardness and peak resistivity values were 1000 and 600 h, respectively. The hardness and resistivity decreased with further natural aging time after reaching the peak values. When GP zones are transformed into stable precipitates, the supersaturation of the solid solution reduces and electron scattering will not be as effective as before. Therefore, a decrease in resistivity of the WQ alloy occurred with increasing natural aging time. The hardness and electrical resistivity values of the FC alloy were 63 HV and 43 nΩm, respectively, which are lower than those of the WQ alloy. The times to reach peak hardness and peak resistivity of the FC alloy are similar to the WQ alloy; however, the increments of the hardness and electrical resistivity were much lower. Figure 6a, b also show that the increases in hardness

and resistivity of the WQ alloy after aging at 120 °C for 1 h (AA1) are higher than those of the FC alloy. The prolonged aging at 120 °C for 4 h (AA4) further increases the hardness of the WQ alloy, while it does not increase the hardness of the FC alloy.

Figure 7a shows DSC curves during heating of WQ alloys with different aging processes. The WQ alloy exhibits a small hump A (endothermic) at around 120 °C, which is related to the dissolution of GP zones [28] that have been formed during the preparation of the DSC sample. A large endothermic peak A (~120 °C) was observed after natural aging for 1000 h due to the dissolution of GP zones formed during the natural aging process. Figure 8a show a high-resolution TEM image of the GP zones, which are known as Zn–Mg rich clusters and are coherent with the Al matrix [29]. The lattice mismatch between the GP zones and the Al matrix causes the formation of misfit dislocations at the interfaces (Fig. 8b). Thus, it is thought that the increases in the hardness and electrical resistivity values during natural aging of the WQ alloy are due to the formation of coherent GP zones in the supersaturated Al matrix.

Minor endothermic peaks around 195 °C (B), 230 °C (C), and 250 °C (D) observed in the WQ alloys with and without natural aging correspond to the dissolution of  $\eta'$ , transformation of  $\eta'$  into  $\eta$ , and dissolution of  $\eta$  [30, 31], which occur continuously during heating of the DSC samples. Meanwhile, a broad peak B was observed after

**Fig. 6** Influence of natural aging time on hardness and electrical resistivity of **a** WQ and **b** FC alloys. Values of as-extruded alloy and artificially aged alloys are indicated for comparison

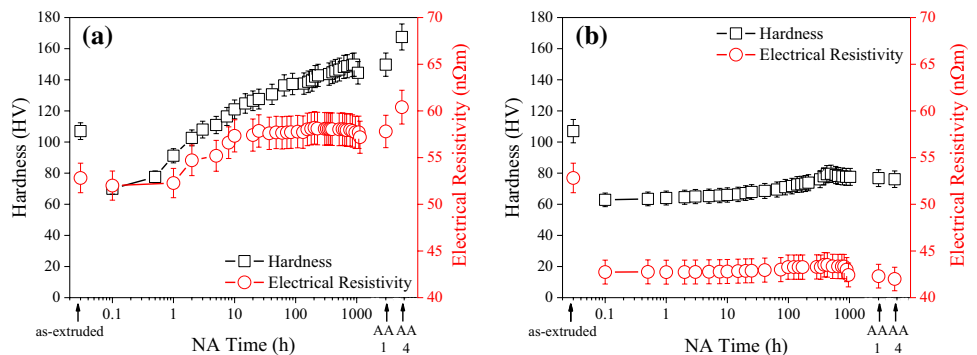


**Fig. 7** Effects of natural aging and artificial aging on DSC curves of **a** WQ and **b** FC alloys

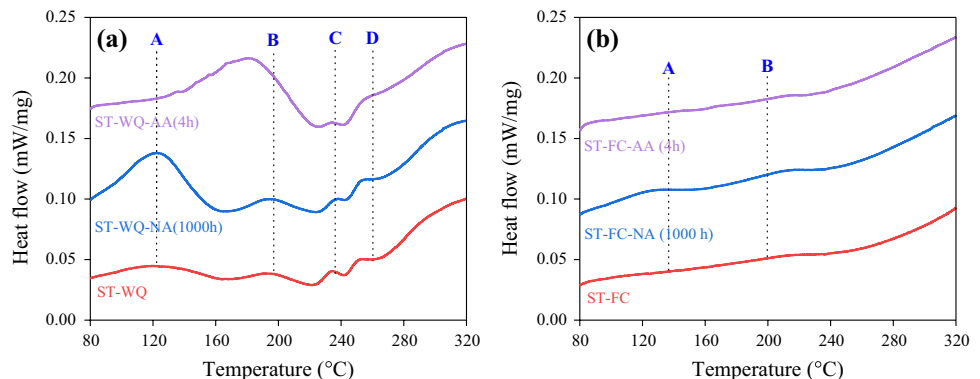
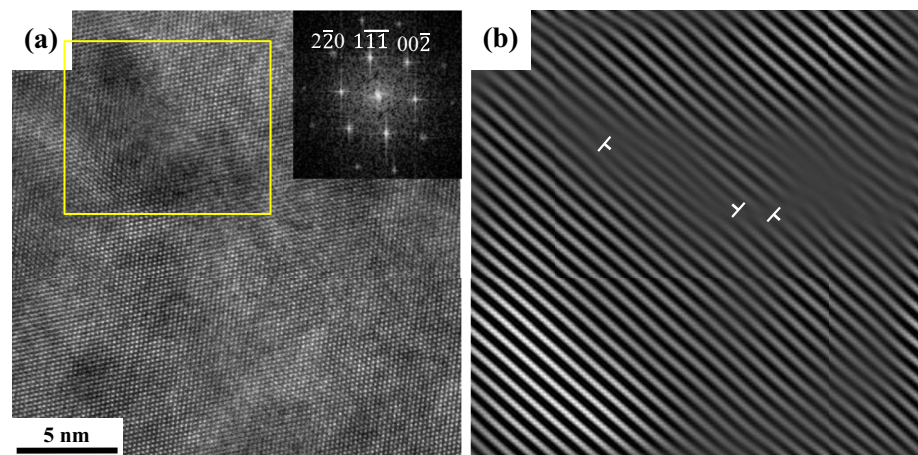


**Fig. 8** **a** HRTEM, FFT, and **b** IFFT results showing the presence of GP zones in WQ alloy



artificial aging of the WQ alloy, indicating that the dissolution of GP zones and the formation of  $\eta''$  and  $\eta'$  precipitates took place at 120 °C. On the other hand, the FC alloy does not exhibit considerable peaks in the DSC curves in any of the aging processes (Fig. 7b). This is because most of the solute atoms have already been utilized in the formation of  $\eta$  precipitates on coarse  $\text{Al}_3(\text{Zr,Ti})$  (formed during solidification), Ti-containing particles, grain boundaries, and grain interior during the slow cooling process.

## 4 Conclusion

1. Partial dissolution of  $\eta$  phase formed during casting took place during prolonged solution treatment at 450 °C. Fine  $\text{L}_{12}$ -type  $\text{Al}_3(\text{Zr,Ti})$  dispersoids with sizes of approximately 20 nm and relatively large ( $\sim 100$  nm) Ti-rich particles were formed during extrusion and/or solution treatment processes.
2. During slow cooling of FC alloy, the precipitation of  $\eta$  phases occurs on coarse  $\text{Al}_3(\text{Zr,Ti})$  particles, Ti-rich particles, grain boundaries, and grain interior. On the other hand,  $\eta$  phase was not observed in the WQ alloy with high cooling rate. The cooling rate from the solution treatment temperature did not change the grain structure, which consists of large elongated (unrecrystallized) grains and fine (recrystallized) grains.
3. The hardness and resistivity of the WQ alloy increased to 150 HV and 58 n $\Omega$ m, respectively, after 1000 h of natural aging due to the formation of coherent GP zones in the Al matrix. In the FC alloy, the formation of GP zones was impossible during the natural aging process due to the lower solute content available in the Al matrix; this ultimately resulted in low hardenability of the alloy.

**Acknowledgements** This work was supported by the Strategic Materials Program (No. 10062304) of the Ministry of Trade, Industry and Energy, Republic of Korea, and the Fundamental Research Program (PNK5990) funded by the Korea Institute of Materials Science.

## References

1. P.A. Rometsch, Y. Zhang, S. Knight, *Trans. Nonferrous Met. Soc. China* **24**, 2003–2017 (2014)
2. B. Milkereit, M.J. Starink, *Mater. Des.* **76**, 117–129 (2015)
3. P. Schloth, A. Deschamps, C.A. Gandin, J.M. Drezet, *Mater. Des.* **112**, 46–57 (2016)
4. J. Lee, H. J. Bong, D. Kim, Y. Lee, Y. Choi, M. Lee, *Met. Mater. Int.* (2019). <https://doi.org/10.1007/s12540-019-00353-9>
5. B.J. Jang, H.S. Park, M.S. Kim, M. Lee, *Met. Mater. Int.* **24**, 1249–1255 (2019)
6. P. Schloth, J.N. Wagner, J.L. Fife, A. Menzel, J.M. Drezet, H. Van Swygenhoven, *Appl. Phys. Lett.* **105**, 101908 (2014)
7. P. Schloth, A. Menzel, J.L. Fife, J.N. Wagner, H. Van Swygenhoven, J.M. Drezet, *Scr. Mater.* **108**, 56–59 (2015)
8. G. Sha, A. Cerezo, *Acta Mater.* **53**, 907–917 (2005)
9. J.L. Cavazos, R. Colás, *Mater. Sci. Eng. A* **363**, 171–178 (2003)
10. D. Godard, P. Archambault, E. Aeby-Gautier, G. Lapasset, *Acta Mater.* **50**, 2319–2329 (2002)
11. A. Deschamps, G. Texier, S. Ringeval, L. Delfaut-Durut, *Mater. Sci. Eng. A* **501**, 133–139 (2009)
12. S. Liu, W. Liu, Y. Zhang, X. Zhang, Y. Deng, *J. Alloys Compd.* **507**, 53–61 (2010)
13. A. Deschamps, Y. Brechet, *Scr. Mater.* **39**, 1517–1522 (1998)
14. A. Deschamps, Y. Brechet, *Mater. Sci. Eng. A* **251**, 200–207 (1998)
15. Murat Tiriyakioglu, Jeremy S. Robinson, Paul D. Eason, *Mater. Sci. Eng. A* **618**, 22–28 (2014)
16. P. Priya, D.R. Johnson, M.J.M. Krane, *Comput. Mater. Sci.* **139**, 273–284 (2017)
17. P. Schloth, Ph.D thesis, École Polytechnique Fédérale de Lausanne (2015)
18. S. Liu, C. Li, S. Han, Y. Deng, X. Zhang, *J. Alloys Compd.* **625**, 34–43 (2015)
19. T. Gao, Y. Zhang, X. Liu, *Mater. Sci. Eng. A* **598**, 293–298 (2014)
20. Y. Wang, Z. Li, B. Xiong, K. Wen, S. Huang, X. Li, Y. Zhang, *Met. Mater. Int.* **25**, 697–704 (2019)

21. H. Yongdong, Z. Xinming, C. Zhiqiang, *Rare Met. Mater. Eng.* **39**, 1135–1140 (2010)
22. N. Ryum, *J. Mater. Sci.* **10**, 2075–2081 (1975)
23. W.H. Tian, M. Nemoto, *Intermetallics* **8**, 835–843 (2000)
24. K.E. Knipling, D.C. Dunand, D.N. Seidman, *Acta Mater.* **556**, 114–127 (2008)
25. K.E. Knipling, D.C. Dunand, D.N. Seidman, *Acta Mater.* **56**, 1182–1195 (2008)
26. F01 Committee, *Test Methods for Measuring Resistivity and Hall Coefficient and Determining Hall Mobility in Single-Crystal Semiconductors*, ASTM International n.d.
27. L.K. Berg, J. Gjønnes, V. Hansen, X.Z. Li, M. Knutson-Wedel, G. Waterloo, D. Schryvers, L.R. Wallenberg, *Acta Mater.* **49**, 3443–3451 (2001)
28. J. Buha, R.N. Lumley, A.G. Crosky, *Mater. Sci. Eng. A* **492**, 1–10 (2008)
29. W.X. Shu, L.G. Hou, C. Zhang, F. Zhang, J.C. Liu, J.T. Liu, L.Z. Zhuang, J.S. Zhang, *Mater. Sci. Eng. A* **657**, 269–283 (2016)
30. D.K. Xu, P.A. Rometsch, N. Birbilis, *Mater. Sci. Eng. A* **534**, 234–243 (2012)
31. T.-F. Chung, Y.-L. Yang, B.-M. Huang, Z. Shi, J. Lin, T. Ohmura, J.-R. Yang, *Acta Mater.* **149**, 377–387 (2018)

**Publisher's Note** Springer Nature remains neutral with regard to jurisdictional claims in published maps and institutional affiliations.